

# Comparative Analysis of the Ten-Step Phase Shifting Technique and StressUnet for Photoelastic Stress Analysis

F. Bullard

L3 Advanced Laboratory, Department of Physics, Durham University

Submitted: 9 January 2024, Date of Experiment: Oct.- Dec. 2023

Understanding how objects behave under stress is crucial in many areas of engineering and materials science, spanning applications from aerospace to bio-engineering. Several numerical methods of stress analysis for complex structures exist, but they are computationally intensive and, therefore, expensive to run. A cheaper, quicker and simpler alternative to such methods is therefore required. Such an alternative is the experimentally-based process of digital photoelasticity. In this report, two methods of digital photoelasticity are investigated: the analytical ten-step phase-shifting technique based on Jones calculus (Ramji and Ramesh, 2008), and StressUnet, a convolutional neural network based on the U-Net architecture (Zhao et al., 2022). The simplicity and low time requirement of stress analysis with StressUnet compared to stress analysis with the phase-shifting technique are highlighted. Both methods are shown to perform inconsistently when evaluated on experimentally obtained data, but StressUnet is shown to perform robustly when evaluated on a large, diverse set of computer-generated data. Experimental setup improvements for both methods are proposed, implementing the adaptive quality guided phase unwrapping algorithm (Ramji, 2010) and increasing the number of training epochs are suggested as improvements to the phase-shifting technique and StressUnet, respectively.

## I. INTRODUCTION

Stress is a physical quantity that describes the magnitude of the forces present in a material. Stress can be split into shear stress and normal stress, quantifying the magnitude of the forces acting parallel and normal to the material surface, respectively [1]. High stress can result in a material failing. For ductile materials such as aluminium, copper and steel, failure occurs when they exceed their elastic range and undergo permanent deformation. The Tresca criterion states that ductile failure occurs when the maximum shear stress  $\tau_{\max}$  exceeds a material-specific critical value [2]. Ductile materials are used in a broad range of fields including aerospace and bio-engineering [3, 4]. To ensure components built out of ductile material don't fail under reasonable stress and to build components more resistant to stress, it is, therefore, key to predict  $\tau_{\max}$  throughout their structure.

Most components are too complex in shape for  $\tau_{\max}$  to be predicted analytically over the whole field. As such, mathematical models and computational simulations, such as the finite element method, have been developed to predict  $\tau_{\max}$  numerically, but they are complicated to set up and require expensive computing hardware to run [5].

Photoelasticity, first discovered by Brewster in 1815, is the phenomenon of stress-induced birefringence [6]. Photoelastic stress analysis, referred to hereafter as photoelasticity, was pioneered in the mid-20th century by Frocht [7, 8]. Initially, experimental frameworks were too slow and results were too subjective for photoelasticity to achieve mass adoption amongst engineers, but, with the rapid development of digital image processing, digital photoelasticity has emerged over the last thirty years as a viable low-cost technique for stress analysis [9].

The ten-step Phase Shifting Technique (PST), proposed by Ramji and Ramesh in 2008, has become a standard technique in digital photoelasticity. It combines the four-step plane polariscope-based approach to isoclinic evaluation proposed by Brown and Sullivan in 1990 with a six-step circular polariscope-based approach to isochromatic evaluation [10, 11]. The terms polariscope, isoclinic and isochromatic are defined in Section II.

Deep learning is a subset of machine learning based on artificial neural networks. It allows computational mod-

els made of many processing layers to predict complex behaviour with multiple levels of abstraction [12]. Over the past three decades, deep learning methods have transformed a wide range of fields, including natural language processing, speech recognition, image segmentation, drug discovery and many more. Convolutional neural networks are a type of deep neural network designed to process data in arrays. Frequently used to extract information from images, they work by applying a series of filter convolutions and scaling operations to the input image and are good at identifying fine features. Once designed and trained, deep learning models produce results quickly and can often be run on generic personal computers. In 2020, Briñez-De-Leon et al. proposed PhotoelastNet, a convolutional neural network, and showed that it could be used to automatically quantify stress maps from isochromatic images [13]. This was an exciting development in digital photoelasticity, as it promised to be a low-cost, quick and simple alternative to the more complicated phase-shifting technique.

U-Net, proposed by Ronneberger et al. (2015) for biomedical image segmentation, is an extension of the standard convolutional neural network that combines both fine-feature and spatial information to aid prediction [14]. Zhao et al. (2022) built on the work of Briñez-De-Leon et al. (2020), presenting StressUnet, a U-Net-based deep learning model with an added physical constraint module. They demonstrated that it achieved better accuracy than PhotoelastNet and required less time and data to train [15].

In this report, two techniques for digital photoelasticity, the ten-step phase shifting technique and StressUnet without the physical constraint module, are compared. Each technique is used to produce whole field maps of the maximum shear stress  $\tau_{\max}$  for a circular disc and ring under diametric compression. StressUnet is also evaluated on a large set of computer-simulated isochromatic images. We expect the ten-step PST to be time-consuming, but produce accurate stress maps, whereas StressUnet should be much faster but produce less reliable results. We find that each technique produces accurate results in some cases, and inaccurate results in others, and suggest ways in which the techniques and data collection process could be improved.

## II. THEORY

Birefringence is the property of some molecularly ordered, transparent materials to have a refractive index that varies for different polarisations of light. Some materials, such as polymers, are temporarily birefringent, and others, such as crystals, are permanently birefringent. Waveplates are optical devices manufactured out of permanently birefringent material in such a way that they alter the polarisation of light travelling through them. To quantify this behaviour, consider a beam of unpolarised monochromatic light of wavelength  $\lambda$  travelling through a waveplate of thickness  $h$ . We can think of this unpolarised beam as made up of two plane-polarised beams, beam 1 and beam 2, with mutually perpendicular oscillations. The refractive index in the waveplate is different for each beam. Calling these refractive indices  $n_1$  and  $n_2$ , the beams travel through the waveplate at speeds  $v_1$  and  $v_2$  given by

$$v_1 = \frac{c}{n_1} \quad \text{and} \quad v_2 = \frac{c}{n_2} \quad (1)$$

where  $c$  denotes the speed of light in a vacuum. Hence, beams 1 and 2 exit the waveplate with a phase difference  $\delta$ , given by

$$\delta = \frac{2\pi h}{\lambda} (n_1 - n_2). \quad (2)$$

Light with a phase difference of 0 or  $\pi$  is linearly polarised, whereas light with a phase difference of  $\pi/2$  or  $3\pi/2$  is circularly polarised. Hence, in altering the phase difference, a waveplate alters the polarisation state of light through it. A quarter waveplate is a popular waveplate instance that imparts a  $\pi/2$  phase difference on incident light. Linearly polarised light incident on a quarter waveplate results in circularly polarised light, and circularly polarised light incident on a quarter waveplate results in linearly polarised light. Equation (2) shows that phase difference is related to wavelength, therefore quarter waveplates only impart an exactly  $\pi/2$  phase difference on light at a specific wavelength, called the design wavelength. Phase difference diverges from  $\pi/2$  for light with a wavelength far from the design wavelength. Waveplates have two axes often labelled fast (F) and slow (S). Axes F and S are orthogonal and have the minimum and maximum refractive indices, respectively [16].

Photoelastically sensitive materials exhibit birefringence when placed under stress. A sample prepared out of photoelastically sensitive material acts as a waveplate with non-uniform birefringence when subject to stress. Consider such a sample, let the stress state at a point be described by orthogonal principal stresses  $\sigma_1$  and  $\sigma_2$  and let the refractive indices corresponding to vibrations parallel to these principal stresses be  $n_1$  and  $n_2$ . We define the stress-optic coefficient  $C$  for the material, such that

$$n_1 - n_2 = C(\sigma_1 - \sigma_2), \quad (3)$$

and rewrite Equation (2) to determine the phase difference  $\delta$  in terms of principal stress difference, giving

$$\delta = \frac{2\pi h C}{\lambda} (\sigma_1 - \sigma_2). \quad (4)$$

For simplicity,  $\sigma_1$  and  $\sigma_2$  are chosen such that  $(\sigma_1 - \sigma_2)$  is always positive. Unlike the principal stress difference,

the phase difference is modulated, meaning a phase difference of  $\delta$  is indistinguishable from a phase difference of  $\delta + 2\pi n$ , where  $n$  is some integer. If the absolute phase difference of light through scale models of large complex structures constructed out of photoelastically sensitive materials can be measured, then the stress distribution in the original structure can, therefore, be deduced [17]. The absolute phase difference, from which the absolute stress distribution is deduced, is determined via phase unwrapping, discussed in Section IV B.

The general optical arrangement used in photoelasticity is called a polariscope. Two variations of the generic polariscope are used: the plane polariscope and the circular polariscope. The plane polariscope, shown in Fig. 1, consists of a light source, two plane polarising filters referred to as the polariser and analyser, a sample of photoelastic material placed under stress between the polariser and the analyser, and an image sensor. The circular polariscope, shown in Fig. 2, is similar to the plane polariscope, but with the addition of two quarter-waveplates, one placed in between the sample and the polariser, and one in between the sample and the analyser. A dark-field polariscope has the polariser and analyser aligned perpendicular to each other and a light-field polariscope has the polariser and analyser aligned in parallel.

Using Jones calculus to trace the polarisation of light through a dark-field linear polariscope, it can be shown that the intensity of light transmitted  $I_p$  is given by

$$I_p = I_a \sin^2 \frac{\delta}{2} \sin^2 2\theta, \quad (5)$$

where  $I_a$  gives the intensity of incident light,  $\delta$  gives the phase difference, and  $\theta$  gives the angle of the slow axis in the sample relative to a set of axes. Connected regions of zero intensity are called dark fringes. By Equation (5), many possible values of  $\delta$  and  $\theta$  yield zero intensity. Dark fringes due to the first term,  $\sin^2 \frac{\delta}{2}$ , are called isochromatics and are observed at points where the principal stress difference  $(\sigma_1 - \sigma_2)$  is such that the phase difference  $\delta$  is a multiple of  $2\pi$ . By Equation (4), isochromatic contours are lines of constant  $(\sigma_1 - \sigma_2)$ . Dark fringes due to the second term,  $\sin^2 2\theta$ , are called isoclinics and are observed at points where one of the principal stress directions coincides with the direction of oscillation of incident plane polarised light. The observed pattern in a plane polariscope is the superposition of isoclinic and isochromatic fringes. Points at which all isoclinics merge are called isotropic points. At an isotropic point, every direction is a principal stress direction and the principal stress difference is zero. Isotropic points have an absolute phase difference  $\delta$  of zero and are key in determining the absolute phase difference over the whole field, as discussed in Section IV B.

Similarly to the linear polariscope, it can be shown with Jones calculus that the intensity of light transmitted from a dark-field circular polariscope is given by

$$I_d = I_a \sin^2 \frac{\delta}{2}, \quad (6)$$

and the intensity of light from a light-field circular polariscope can be shown to be given by

$$I_l = I_a \cos^2 \frac{\delta}{2}. \quad (7)$$

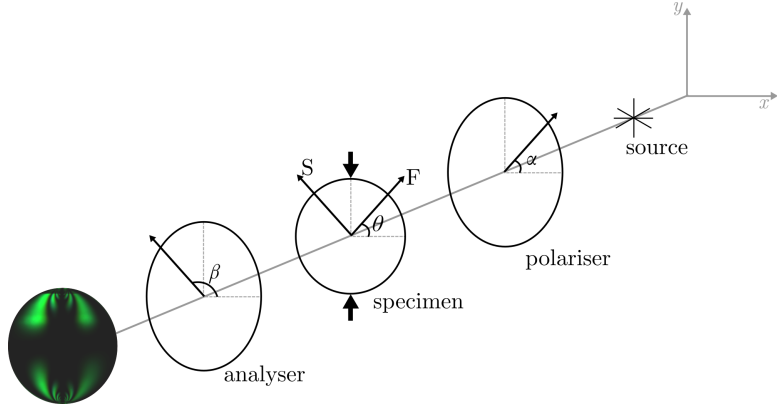


**FIG. 1:** Plane polariscope. The experimental setup used in the first four steps of the ten-step PST.

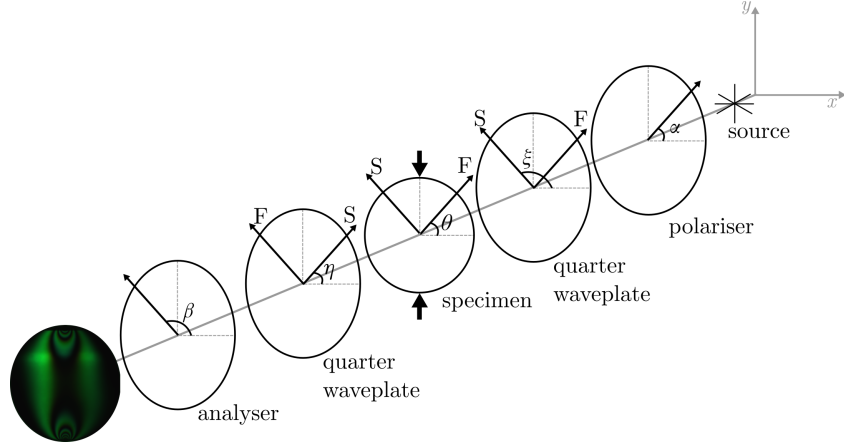


**FIG. 2:** Circular polariscope. The experimental setup used in the final six steps of the ten-step PST.

Equations (6) and (7) show implicitly that the pattern observed in a circular polariscope contains isochromatic fringes only. Intuitively, this can be explained by the circular polarisation of light incident on the sample in a circular polariscope meaning the principal stress direction never coincides with the direction of polarisation, so isoclinic fringes never form.

To extract stress information from the isochromatic fringe patterns, we rewrite Equation (4) in terms of isochromatic fringe-order  $N$ , giving

$$N = \frac{\delta}{2\pi} = \frac{hC}{\lambda}(\sigma_1 - \sigma_2). \quad (8)$$

From Mohr's circle, the maximum shear stress  $\tau_{\max}$  is given in terms of the principal stress difference as

$$\tau_{\max} = \frac{1}{2}(\sigma_1 - \sigma_2) \quad (9)$$

[18]. Rearranging and substituting into Equation (9), we find the maximum shear stress is given by

$$\tau_{\max} = \frac{NF_\sigma}{2h}, \quad (10)$$

where  $F_\sigma$  denotes the material stress-fringe value,

$$F_\sigma = \frac{\lambda}{C}. \quad (11)$$

It should be noted that the relationship between  $F_\sigma$  and principal stress difference given implicitly as linear by Equation

(10) becomes non-linear at higher stress levels. In this report, we assume linearity holds in all cases.  $F_\sigma$  varies from batch to batch and over time, so it must be calculated at the time of the experiment for each sheet of material [9].

### III. EXPERIMENTAL SETUP

In our investigation, a 24 V, 250 W projector lamp with an incandescent bulb was used as a light source, a softbox and several layered sheets of tissue paper were used illuminate the sample evenly, a Canon EOS 760D digital SLR with Canon EF-S 18-55MM F/3.5-5.6 IS II lens was used with ISO-200 and an exposure time of 1/3s to capture the images, and a modified car jack was used to place the samples under compressive stress. Exposure time and ISO were selected to minimise image noise whilst balancing exposure brightness and time needed to collect data. The design wavelength of the quarter waveplates we used was not recorded, but similar products online range from 560 nm to 588 nm, with transmission greater than 90% in the range 450 nm to 700 nm [19].

Approximately monochromatic light was used for the ten-step phase-shifting technique, and white light was used to test StressUnet. The monochromatic light was obtained by combining a yellow and a cyan colour filter and taking data from the green channel only. The relative spectral response of the camera we used was not available online; instead, the relative spectral response for a similar model is illustrated alongside the relative spectral content of a typical

**TABLE I:** Optical arrangement and intensity equations calculated with Jones Calculus for ten-step phase shifting techniques.

$\alpha$	$\xi$	$\eta$	$\beta$	Intensity Equation
$\pi/2$	-	-	0	$I_1 = I_b + I_a \sin^2 \frac{\delta}{2} \sin^2 2\theta$
$5\pi/8$	-	-	$\pi/8$	$I_2 = I_b + \frac{I_a}{2} \sin^2 \frac{\delta}{2} (1 - \sin 4\theta)$
$3\pi/4$	-	-	$\pi/4$	$I_3 = I_b + I_a \sin^2 \frac{\delta}{2} \cos^2 2\theta$
$7\pi/8$	-	-	$3\pi/8$	$I_4 = I_b + \frac{I_a}{2} \sin^2 \frac{\delta}{2} (1 + \sin 4\theta)$
$\pi/2$	$3\pi/4$	$\pi/4$	$\pi/2$	$I_5 = I_b + \frac{I_a}{2} (1 + \cos \delta)$
$\pi/2$	$3\pi/4$	$\pi/4$	0	$I_6 = I_b + \frac{I_a}{2} (1 - \cos \delta)$
$\pi/2$	$3\pi/4$	0	0	$I_7 = I_b + \frac{I_a}{2} (1 - \sin 2\theta \sin \delta)$
$\pi/2$	$3\pi/4$	$\pi/4$	$\pi/4$	$I_8 = I_b + \frac{I_a}{2} (1 + \cos 2\theta \sin \delta)$
$\pi/2$	$\pi/4$	0	0	$I_9 = I_b + \frac{I_a}{2} (1 + \sin 2\theta \sin \delta)$
$\pi/2$	$\pi/4$	$3\pi/4$	$\pi/4$	$I_{10} = I_b + \frac{I_a}{2} (1 - \cos 2\theta \sin \delta)$

*Note.* From ‘‘Developments in Photoelasticity: a Renaissance’’ (ch. 3, p. 6), by K. Ramesh, 2021, IOP Publishing (<https://iopscience.iop.org/book/mono/978-0-7503-2472-4>).

incandescent bulb, the transmission fraction of the yellow and cyan colour filters, and the resultant spectral content of the monochromatic and colour images in Fig. 3. The resultant monochromatic spectral content was calculated as the normalised product of the yellow and cyan colour filter transmission fractions, the incandescent bulb spectral content, and the green channel spectral response. The resultant white light spectral content was calculated as the normalised product of the spectral content of the incandescent bulb and the sum of the spectral responses of the red, green and blue channels. To best match the peak wavelength of the monochromatic light to the design wavelength of the quarter waveplates and minimise the error in  $\delta$ , yellow and cyan colour filters were chosen together to give approximately monochromatic green light with peak wavelength ( $550 \pm 50$ ) nm and a narrow wavelength range; error calculation is described in appendix A.

A polymethyl methacrylate (PMMA) disc and a PMMA ring were used as samples to investigate each technique. Both had thickness  $h$  of 12 mm. The disc had radius 5 cm, and the ring had inner and outer radii 2.5 cm and 5 cm, respectively. To avoid errors due to residual stresses in the material, each specimen was examined under zero load before use and was used only once.

#### IV. THE TEN-STEP PHASE SHIFTING TECHNIQUE

##### A. Background

The optical arrangements for each of the ten steps are listed alongside the formulae for their intensity derived from Jones calculus in Table I (K. Ramesh, 2021). The incident and background intensities are indicated by  $I_a$  and  $I_b$ , respectively. The ten optical arrangements were chosen carefully, keeping the quarter waveplates crossed where possible to minimise the influence of quarter waveplate misalignment [9].

Derived from Jones calculus, the wrapped isoclinic pa-

rameter  $\theta_c$  is given by

$$\begin{aligned}\theta_c &= \frac{1}{4} \tan^{-1} \left( \frac{I_4 - I_2}{I_3 - I_1} \right) \\ &= \frac{1}{4} \tan^{-1} \left( \frac{I_a \sin^2 \frac{\delta}{2} \sin(4\theta)}{I_a \sin^2 \frac{\delta}{2} \cos(4\theta)} \right),\end{aligned}\quad (12)$$

where  $I_1, I_2, I_3, I_4$  are the intensities recorded at each respective step.  $\theta_c$  is undefined where  $\sin^2 \delta/2$  is equal to 0, implying the isoclinic parameter is undefined at isochromatic fringes. To produce continuous phase maps,  $\theta_c$  was set to 0 at such points. The subscript c indicates that the principal value of the inverse tangent function is taken, so  $\theta_c$  has values between  $-\pi/4$  and  $\pi/4$ .

$\theta_c$  is unwrapped to produce  $\theta$ , which is used alongside the intensities recorded in the final six steps  $I_5, I_6, I_7, I_8, I_9, I_{10}$  to determine the isochromatic parameter  $\delta_c$ , where

$$\delta_c = \tan^{-1} \left( \frac{(I_9 - I_7) \sin 2\theta + (I_8 - I_{10}) \cos 2\theta}{I_5 - I_6} \right). \quad (13)$$

$\delta_c$  is wrapped between  $-\pi$  and  $\pi$ . Unwrapping  $\delta_c$  and dividing by  $2\pi$  yields isochromatic fringe order  $N$ , from which the maximum shear stress  $\tau_{\max}$  can be obtained via Equation (10).

Determining  $\delta_c$  with the wrapped isoclinic parameter  $\theta_c$  is possible, but areas of isoclinic fringe order greater than zero produce ambiguous zones that are difficult to unwrap. An unwrapping algorithm, described in Section IV B, is used to produce  $\theta$  which has values between  $-\pi/2$  and  $\pi/2$ .

The maximum shear stress  $\tau_{\max}$  is calculated from the isochromatic fringe-order  $N$  via Equation (10), using the material stress-fringe value  $F_\sigma$  determined for the batch of material used. From the principle of superposition in solid mechanics and applying Boussinesq’s solution for a semi-infinite plate subjected to a concentrated vertical load, it can be shown that a circular disc with diameter  $D$  under diametral compression by load force  $P$  has material stress-fringe value given by

$$F_\sigma = \frac{8P}{\pi D N_c}, \quad (14)$$

where  $N_c$  denotes the fringe order at the centre of the disc.

##### B. Unwrapping Isoclinics and Isochromatics

As the inverse tangent function is multi-valued, the isoclinic and isochromatic parameters obtained from the ten-step PST are wrapped in the ranges  $[-\pi/4, \pi/4]$  and  $[-\pi, \pi]$ , respectively. The isoclinic parameter  $\theta_c$  must be unwrapped for use in the determination of the isochromatic parameter  $\delta_c$ , and  $\delta_c$  must be unwrapped to obtain the fringe order  $N$  from which the Equation (10) is used to calculate maximum shear stress  $\tau_{\max}$ .

The unwrapped isoclinic parameter  $\theta$  at a point is related to the wrapped isoclinic parameter  $\theta_c$  by

$$\theta = \theta_c + n \frac{\pi}{2}, \quad n \in \mathbb{Z}, \quad (15)$$

where integer  $n$  is to be determined. The isochromatic fringe order  $N$  is related to the wrapped isochromatic parameter  $\delta_c$  by

$$2\pi N = \delta_c + 2m\pi, \quad m \in \mathbb{Z}, \quad (16)$$

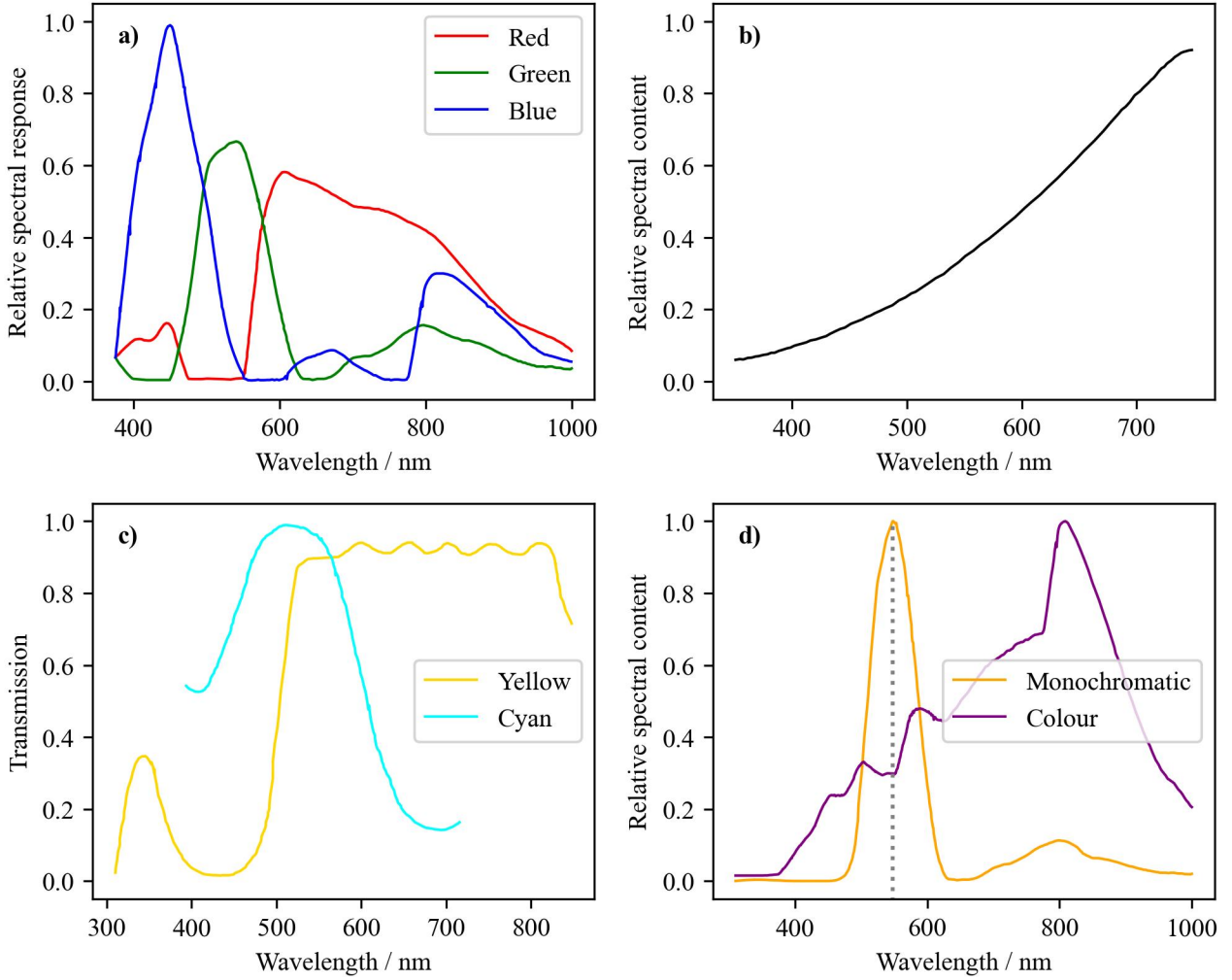


**FIG. 3:** Spectral content of components. **a)** Relative spectral response of Canon EOS 40D digital SLR; **b)** relative spectral content of a typical incandescent bulb; **c)** transmission fraction of yellow and cyan colour filters; **d)** relative spectral content of resultant colour and monochromatic light [20–22]. The camera and colour filter graphs were obtained from their manufacturers.

where integer  $m$  is to be determined.

To unwrap the isoclinics and isochromatics, the phase unwrapping algorithm proposed by Macy (1983) was implemented. Representing the wrapped phase maps as two-dimensional arrays, we define the neighbours of a pixel with coordinates  $(j, k)$  as  $(j - 1, k)$ ,  $(j, k - 1)$ ,  $(j + 1, k)$  and  $(j, k + 1)$ . To keep the following formulae concise,  $i$  and  $i + 1$  are used to denote neighbouring pixels.

By the sampling theorem, the highest possible change in phase between two neighbouring pixels is less than half the phase range. Hence, the differences in unwrapped isoclinic phase and fringe order between two neighbouring pixels  $i$ ,  $i + 1$  obey the inequalities

$$-\frac{\pi}{4} < \theta_{i+1} - \theta_i < \frac{\pi}{4} \quad (17)$$

and

$$-\frac{1}{2} < N_{i+1} - N_i < \frac{1}{2}, \quad (18)$$

respectively. Rearranging Equations (17) and (18) and substituting in the formulae for  $\theta$  and  $N$  from Equations (15) and (16), we arrive at the recurrence relations

$$\theta_{i+1} = \left( ((\theta_c)_i - \theta_i) \bmod \frac{\pi}{2} \right) + \theta_i - \frac{\pi}{4} \quad (19)$$

and

$$N_{i+1} = \left( \left( \frac{\delta_i}{2\pi} - N_i \right) \bmod 1 \right) + N_i - \frac{1}{2}, \quad (20)$$

where  $\bmod$  denotes the modulo operation.

To unwrap the isoclinics and isochromatics, a mask  $M$  was prepared for each shape using the GNU Image Manipulation Software (GIMP), where

$$M_{ij} = \begin{cases} \infty & \text{if } (i, j) \text{ in shape field} \\ -\infty & \text{otherwise.} \end{cases}$$

An array queue was initialised containing the seed points from which to start unwrapping. Seed points from the same fringe were selected manually for isoclinic unwrapping. Isotropic points were selected for isochromatic unwrapping. Algorithm 1 was applied to each wrapped phase-map. The UNWRAP function represents Equation (19) or (20) for isoclinic or isochromatic unwrapping, respectively [23].

The unwrapping algorithm described above is very sensitive to noise. To reduce errors in unwrapping, care was taken to manually select seed points in areas of low noise and a median filter was applied to all wrapped phase maps.

**Algorithm 1:** Unwrapping algorithm based on Macy's method.

---

**Data:** wrapped: 2d Array, mask: 2d Array, seeds: Array  
 unwrapped  $\leftarrow$  mask;  
**foreach** seed in seeds **do**  
 | unwrapped[seed]  $\leftarrow$  wrapped[seed];  
**end**  
 queue  $\leftarrow$  seeds;  
**while** queue is not empty **do**  
 |  $(x, y) \leftarrow$  pop the first element from queue;  
 | neighbours  $\leftarrow$  [(x-1,y), (x+1,y), (x,y-1), (x,y+1)];  
 | **foreach**  $(i, j)$  in neighbours **do**  
 | | **if** unwrapped[(i,j)] =  $\infty$  **then**  
 | | | unwrapped[(i,j)]  $\leftarrow$  UNWRAP((i,j), (x,y));  
 | | | queue.append((i,j));  
 | | **end**  
 | **end**  
**end**

---

The median filter is a standard noise reduction technique where the pixel value at a point is replaced with the median of a kernel of pixels around it. The size of the kernel is specified when applying the filter; here, a kernel of radius 5px was used.

**C. Identification of isotropic points**

Isotropic points were selected as seed points for isochromatic unwrapping as they are easy to identify and are known to have an isochromatic fringe order of zero. For each sample, the plane polariscope was illuminated with white light, and the polariser was rotated from  $0^\circ$  to  $90^\circ$ , keeping the polariser-analyser system crossed. Images were taken at intervals of  $10^\circ$ , and are presented in Appendix B. Isotropic points were identified by locating the points of zero intensity across all ten images. The isotropic points for the case of the circular disc and ring under diametric compression are indicated in Fig. 4.

**V. THE DEEP LEARNING TECHNIQUE****A. Model Architecture**

The model architecture used is indicated in Fig. 5 (Zhao et al., 2022) and the input and output sizes of each block are listed in Table II (Zhao et al., 2022) [15]. Due to computational limitations, the physical constraint module in StressUnet was omitted.

U-Net is the combination of two paths: the encoding path and the decoding path. The encoding path (encoder) is made up of layers of convolution followed by max-pooling operations. The spatial dimensions of layer outputs are lowered with each successive layer, and high-resolution, low-level characteristics are captured. The decoding path (decoder) is made up of layers of de-convolution. The spatial dimensions of layer outputs are increased over the decoding path, allowing the individual features identified in encoding to be combined into an output image. Skip connections are a key aspect of the U-Net architecture, and are used to connect matching encoding and decoding layers. They enable

**TABLE II:** Encoder and Decoder Parameters of Each Block<sup>a</sup>

Block	Input Size	Output Size
First block	224 * 224 * 3	112 * 112 * 64
Encoder1	112 * 112 * 64	56 * 56 * 64
Encoder2	56 * 56 * 64	28 * 28 * 128
Encoder3	28 * 28 * 128	14 * 14 * 256
Encoder4	14 * 14 * 256	7 * 7 * 512
Centre	7 * 7 * 512	14 * 14 * 512
Decoder4	14 * 14 * 512	28 * 28 * 256
Decoder3	56 * 56 * 128	112 * 112 * 64
Decoder2	112 * 112 * 64	224 * 224 * 64
Decoder1	224 * 224 * 64	224 * 224 * 1

<sup>a</sup> The first two numbers of the size indicate the size of the image and the last number indicates the channels of the image

*Note.* From “Accuracy improvement of demodulating the stress field with StressUnet in photoelasticity,” by W. Zhao et al., 2022, Applied Optics, 61(29), p. 8678 (doi.org/10.1364/AO.464466).

the model to consider local and global information, making the U-Net architecture well-suited to photoelasticity.

The Residual Neural Network (ResNet) backbone was chosen for the encoder to ensure the stability of the model, prevent over-fitting and enhance generalisation ability [24].

For a given isochromatic image, StressUnet generates a predicted stress map by combining the hierarchical stress data obtained by the encoder over multiple scales in the decoder. The magnitude of the predicted stress map is produced assuming a PMMA sample with thickness 0.01 m.

**B. Isochromatic Dataset**

Deep neural networks such as U-Net require a large amount of labelled data to train. Our model was trained and tested on subsets of a large, publicly available set of 101,430 computer-generated isochromatic images and reference stress maps. The dataset contained fringe-stress pairs for a circular disc and three rings under diametric compression, a plate with a hole under axial compression, a rod under punctual bending and distributed bending, and three rings under rotation, as well as cases from other fields such as saliency maps, Gaussian distributions and 3D models. Each case was simulated using theoretical incandescent, fluorescent, white LED and cold white laser spectral contents as well as constant in the visible range, and Sony IMX250, DCU3260 and human vision spectral responses. The dataset was selected for its size and the broad range of photoelasticity cases to achieve high generality after training [13].

**C. Loss function and Training**

The structural similarity (SSIM) index is a popular image quality metric that quantifies the similarity between two images. SSIM was used to compare the similarity between reference and predicted stress maps [25]. For a reference image  $r$  and prediction image  $p$ , the SSIM is given by

$$\text{SSIM}(r, p) = \frac{(2\mu_r\mu_p + C_1)(2\sigma_{rp} + C_2)}{(\mu_r^2 + \mu_p^2 + C_1)(\sigma_r^2 + \sigma_p^2 + C_2)}, \quad (21)$$

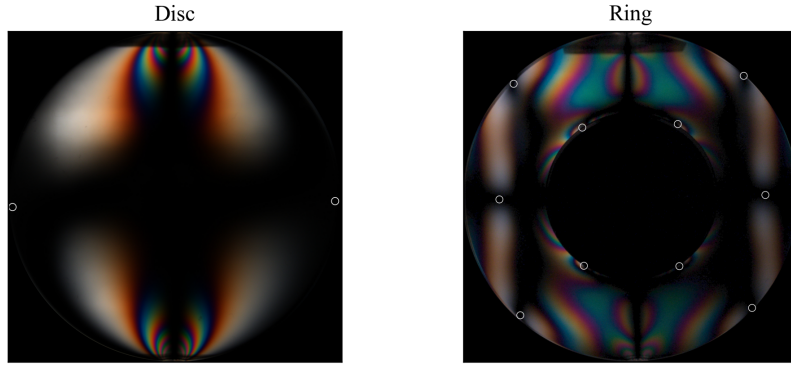


**FIG. 4:** Isotropic points indicated on white-light illuminated linear polariscope images of the circular disc (left) and ring (right) under diametric compression.

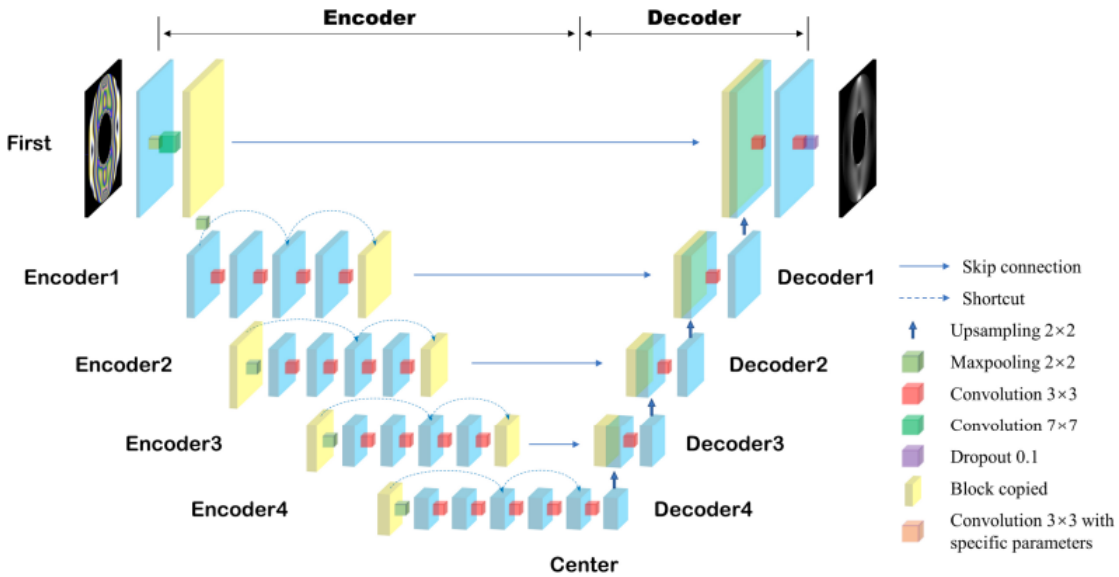


**FIG. 5:** Illustration of the U-Net architecture. *Note.* From “Accuracy improvement of demodulating the stress field with StressUnet in photoelasticity,” by W. Zhao et al., 2022, Applied Optics, 61(29), p. 8678 (doi.org/10.1364/AO.464466).

where

$$\mu_r = \frac{1}{N} \sum_{i=1}^N r_i, \quad (22)$$

$$\sigma_{rp} = \frac{1}{N-1} \sum_{i=1}^N (r_i - \mu_r)(p_i - \mu_p), \quad (23)$$

and

$$\sigma_r = \left( \frac{1}{N-1} \sum_{i=1}^N (r_i - \mu_r)^2 \right)^{\frac{1}{2}}. \quad (24)$$

SSIM captures the structural similarity between the two images, meaning it penalises differences in structural information.

The mean squared error (MSE) between two images estimates the absolute error. MSE is given by

$$\text{MSE}(r, p) = \frac{1}{mn} \sum_{i=1}^m \sum_{j=1}^n (r_{ij} - p_{ij})^2. \quad (25)$$

To train for the identification of both local and global stress patterns, a weighted sum of SSIM and mean square error (MSE) was used as the loss function  $\mathcal{L}$ , given by

$$\mathcal{L} = 1 - \text{SSIM}(r, p) + \lambda \text{MSE}(r, p), \quad (26)$$

where

$$\lambda = \begin{cases} 1 & \text{epoch} \leq 20 \\ 1 + 0.2(\text{epoch} - 20) & \text{epoch} > 20 \end{cases}.$$

Over the first twenty epochs,  $\lambda$  was kept small to allow the model to focus on the general structure.  $\lambda$  was increased for the final four epochs to make the model focus on the fine structure of zones of high stress [15].

10,000 images at even intervals were selected from the dataset to make up the training data, ensuring that each case was included in training. Similarly, a further 2,000 images were selected from the dataset to make up the validation set. The sizes of these data sets were chosen to keep training time low and avoid over-fitting the model without sacrificing model accuracy.

The model was trained over 24 epochs. After each epoch, the model was evaluated on the validation set. If the SSIM

was higher than that of the previous epoch, the model parameters were updated. The Adam optimiser was used as the network optimiser for its low training time and memory requirements [26]. The learning rate was set to  $10^{-4}$  for the first 20 epochs and  $10^{-5}$  for the final 4. A batch size of 128 was used, keeping the required memory and training time manageable whilst minimising over-fitting. PyTorch run on a desktop with an Intel i5 14-Core Processor at 4.80 GHz, 32 GB of memory, and Nvidia GeForce RTX3060Ti GPU was used for all training and testing implementations.

## VI. RESULTS

### A. Ten-Step Phase Shifting Technique

Images were captured as RAW files with the .CR2 file extension to reduce data loss due to compression. The Python library RAWPI was used to import the raw images and convert them to manipulatable arrays.

The isochromatic fringe order over the disc field is plotted in Fig. 6. The central fringe order,  $N_c$ , was determined to be  $2.618 \pm 0.006$ , where the mean of the 10 by 10 kernel at the centre of the fringe image was taken to account for inconsistencies. The uncertainty in  $N_c$  was set as the standard deviation of the kernel, described in Appendix A. The material fringe-stress value  $F_\sigma$  was determined via Equation (14) to be  $(38.2 \pm 0.1)$  kN/m/Fringe and used to calculate the maximum shear stress.

The whole field wrapped isoclinic parameter  $\theta$ , unwrapped isoclinic parameter  $\theta_{\text{unwrapped}}$ , isochromatic parameter  $\delta$  and maximum shear stress  $\tau_{\max}$  obtained from the ten-step PST, unwrapping algorithm and Equation 10 for the disc and ring under diametric compression are shown in Fig. 7. The images taken of each step are presented in Appendix C.

For the disc, the produced phase and stress maps are generally continuous, with noise isolated to the boundary of the disc. The isochromatic parameter appears slightly asymmetric with fringes bulging towards the top left and bottom right. It also shows a small dark area to the left of and above the centre. The stress map shows the top and bottom of the disc to have the highest stress concentration, with lower stress at the centre and lowest at the edges. It is asymmetric with stress higher in the top left and bottom right than the top right and bottom left.

For the ring, all four images show noise at the top.  $\theta_{\text{unwrapped}}$  and  $\delta$  both show rectangular discontinuous sections on the left and right sides of the ring centre. The stress map obtained is noisy, with sharp discontinuities throughout the field. Through the noise, the underlying pattern resembles the reference stress maps for a compressed ring in Fig 8.

### B. Stress Unet

The StressUNET model was evaluated on the validation data set, achieving 0.9780 SSIM overall. The model's maximum shear stress predictions and the SSIM relative to the reference stress maps for six sample isochromatic images selected from the test data set are shown in Fig. 8. The disc and ring images were chosen to allow for effective comparison with experimental data, the dragon image was chosen

to demonstrate how the model performed for more complex shapes. The model successfully predicted the overall stress pattern for each shape, correctly identifying areas of high and low stress. It overestimated the stress at the sides of the rings and predicted a less concentrated stress distribution for the disc. It struggled to predict the finer stress patterns seen in the dragon and at the top and bottom of the rings and disc. The model was less effective at higher compressive forces, with SSIM decreasing from 0.9926 to 0.9752 as maximum stress increased from 12 MPa to 72 MPa.

StressUnet was used to predict the maximum shear stress over the whole field of a circular disc and ring under a range of compressive forces with experimentally obtained isochromatic images cropped to 224 x 224 and converted to the .BMP file format to match the dimensions and format of the training dataset. The disc and ring results are presented in Fig. 9 and 10, respectively. For the disc, the top and bottom were successfully identified by the model as the areas of highest stress. For 0.98 kN and 1.96 kN of compressive force, a similar pattern as in the reference disc stress map in Fig. 8 was predicted. For higher forces, the model's predictions did not match the expected pattern. For the ring under 2.94 kN and 3.92 kN of compressive force, the areas of low and high stress were correctly identified by the model, although stress was overestimated at the sides and underestimated at the bottom. For the ring under 0.98 kN and 1.96 kN of compression, the predictions don't match the expected pattern.

## VII. DISCUSSION

### A. Ten-Step Phase Shifting Technique

Setting up the optical arrangements precisely was time-consuming, and the load  $P$  on the sample varied throughout each experiment. For the ten-step PST, this increased uncertainty in  $F_\sigma$  and thus the produced stress maps. Care was taken to keep the load close to constant, but the car jack did not support fine adjustments. Implementing a more precise loading mechanism such as the servo press used by Ren et al. (2022) would enable  $P$  to be set with more precision and reduce the time between measurements [27].

To obtain accurate, symmetric stress maps, the quarter waveplates had to be perfectly aligned. Available lab time constrained how much care could be taken setting up each arrangement, and so the asymmetries of the disc isochromatic parameter and maximum shear stress were likely caused by quarter wave-plate misalignment. To reduce this error, the quarter wave-plates could be mounted in a rotating frame with marked angle increments, enabling their angles to be set with more precision and in less time.

Unwrapping the isoclinics and isochromatics in the case of the disc and the isoclinics in the case of the ring yielded results closely resembling that of the literature [9]. All three of these unwrapped phase maps featured several narrow horizontal discontinuities where the unwrapping algorithm detected erroneous  $\pi$ -jumps. The ring was more difficult for the algorithm to unwrap. Around the isotropic points to the left and the right of the centre, it produced wide rectangles of zero phase when unwrapping the isoclinics. Unwrapping the isochromatics produced a highly discontinuous stress map. These discontinuities arose where paths unwrapping from different seed points met out of phase as a

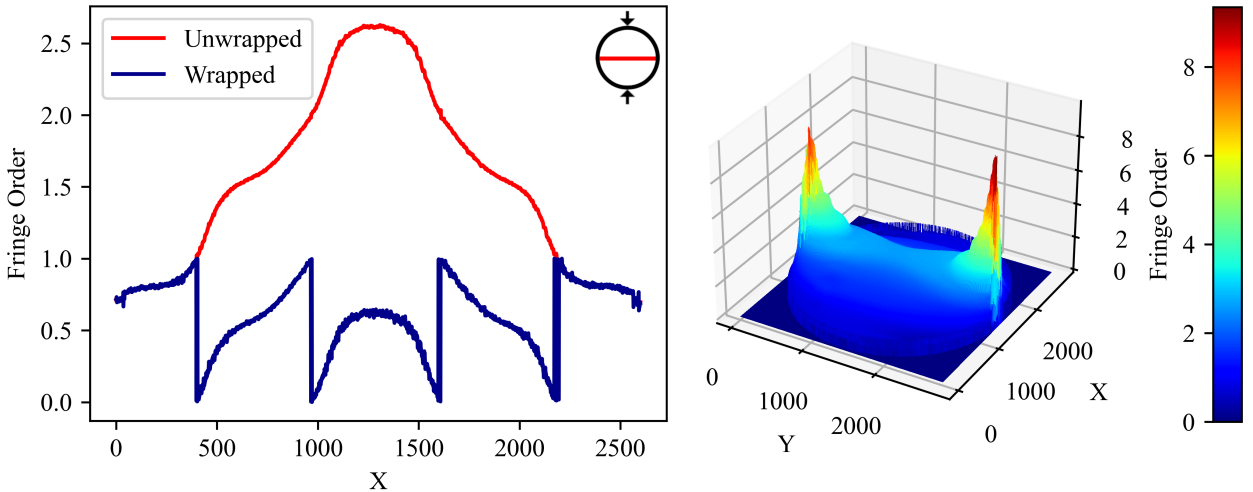


**FIG. 6:** The wrapped and unwrapped fringe order across the horizontal diameter of the disc (left), a three-dimensional plot of fringe order over the disc field (right).

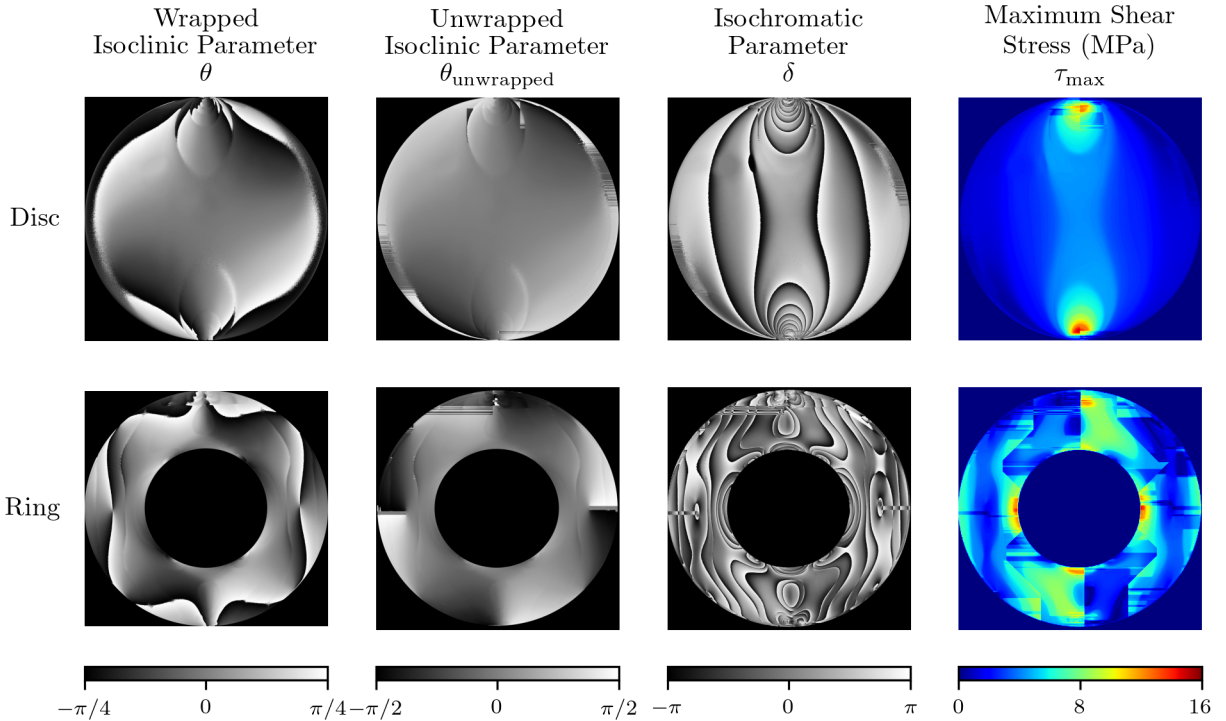


**FIG. 7:** Wrapped isoclinic parameter, unwrapped isoclinic parameter, isochromatic parameter and maximum shear stress obtained for the circular disc and ring under diametric compression.

result of noise in the isochromatic phase map provoking a premature  $\pi$ -jump. The failure of the unwrapping algorithm to unwrap the ring isochromatics suggests it could be improved to better handle the ring and other complex shapes. Ramesh and Ramji (2010) proposed the adaptive quality guided phase unwrapping algorithm (AQGPU) where, instead of unwrapping radially out from the seed points, each unwrapped point is assigned a ‘quality value’ related to the statistical variance of the phase derivatives of its neighbourhood, and the queue is ranked by this quality value such that neighbours of points with high-quality value are unwrapped with higher priority. This algorithm is likely to be more accurate for complex shapes, producing stress maps with fewer discontinuities, but would be much more com-

putationally intensive [28].

## B. StressUnet

Zhao et al. (2022) reported an SSIM of 0.9789 for StressUnet without the constraint module evaluated on the validation set. The discrepancy between our SSIM and theirs is likely due to the fewer epochs we trained over: we expect that our model would have performed as well as theirs had it been trained for the full 60 epochs. They reported a slightly increased SSIM of 0.9790 for StressUnet with the constraint module when evaluated on the same validation set [15].

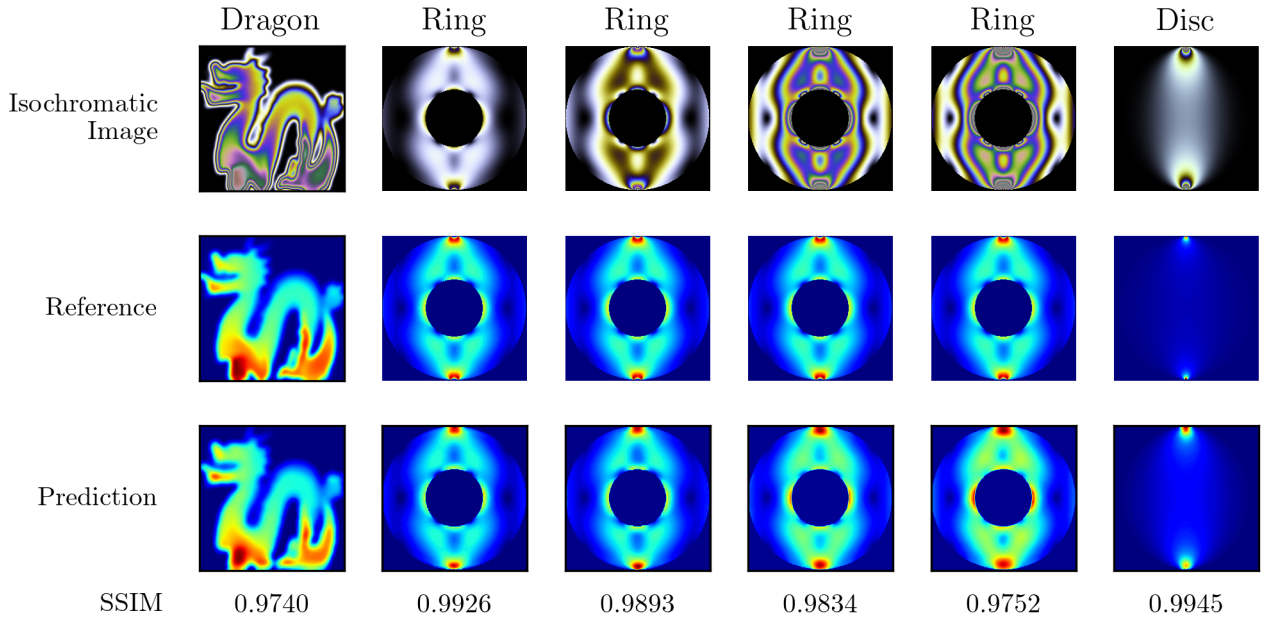


**FIG. 8:** Sample isochromatic images from the data set (first row), reference stress maps (second row), stress maps predicted by StressUNET (third row), structural similarity (SSIM) between reference and prediction (fourth row). The rings are presented in order of increasing compressing force from left to right.

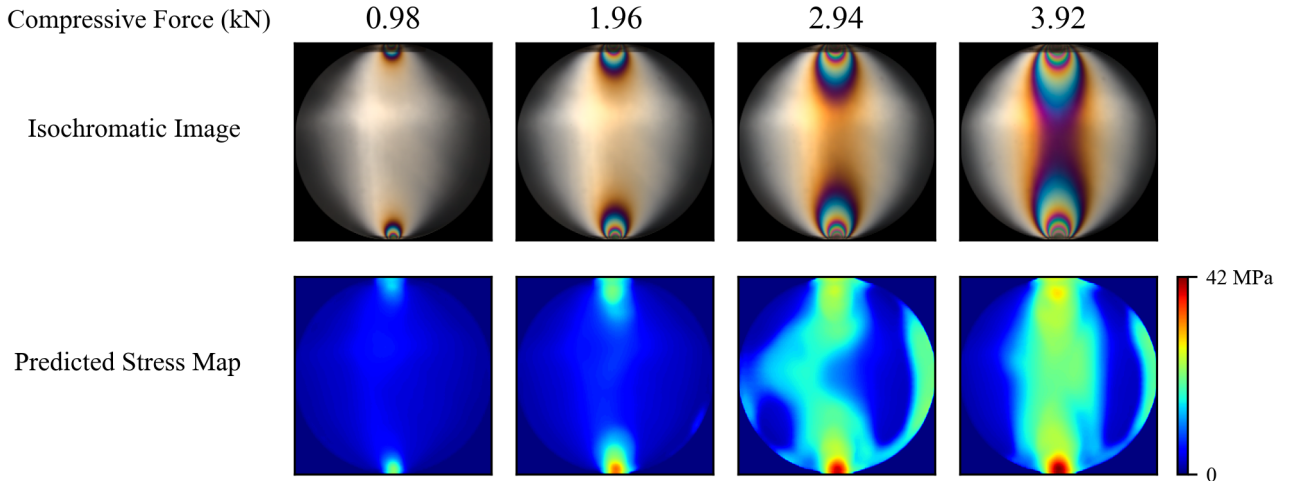


**FIG. 9:** Experimentally obtained isochromatic images for a disc under diametric compression (top) and maps of their maximum shear stress predicted by StressUnet (bottom)

The performance of the StressUnet model when evaluated on our experimentally obtained data was inconsistent. Stress maps obtained for the disc under 0.98 kN and 1.96 kN loads and the ring under 2.94 kN and 3.92 kN loads resembled the reference stress maps in Fig. 8. The remaining four stress maps were inaccurate. The model's robust performance on the validation data set suggests that its performance on the experimentally obtained data is unlikely to be improved significantly by increasing the number of training epochs. Comparing the experimental and theoretical isochromatic images, there are a few clear differences which could instead have been responsible for the inaccuracy of predicted stress maps. The isochromatic images of the disc and ring in Figures 9 and 10 show the lighting was not even across the whole field. This can be seen clearly in the images of the disc, where the upper left quarter ap-

pears brighter than the rest of the field. These images are also less vibrant and have lower contrast than the theoretical images in Fig. 8. Stress maps produced by StressUnet from experimental data could therefore be improved by ensuring the whole field is illuminated uniformly and by applying post-processing to the isochromatic images to bring them closer in appearance to the training data. In future investigations, the use of different light sources such as a cold white laser and different specimen thicknesses could also be investigated to better replicate the theoretical isochromatic images.

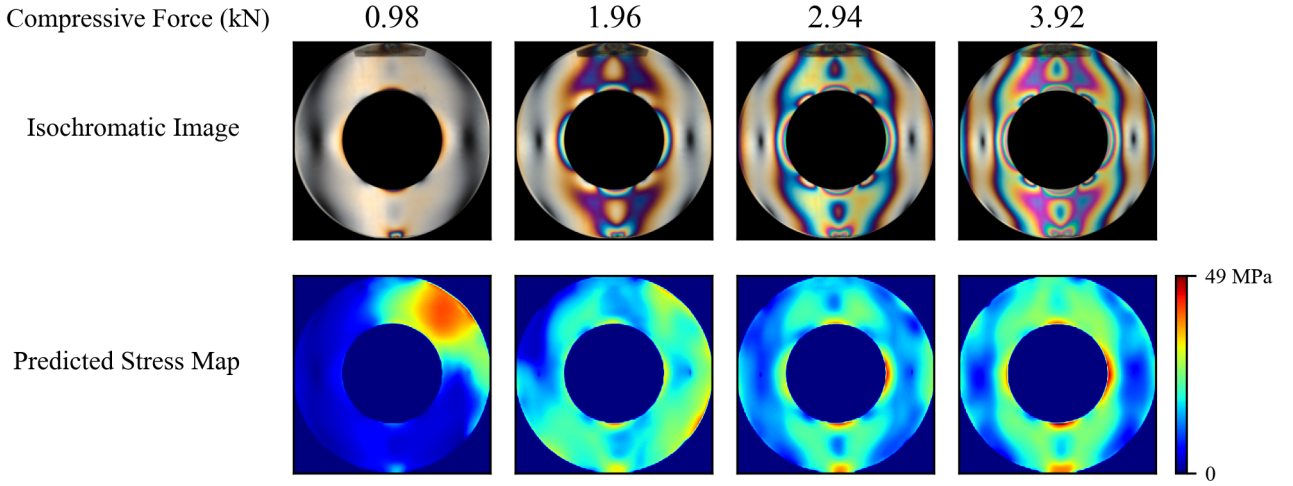


**FIG. 10:** Experimentally obtained isochromatic images for a ring under diametric compression (top) and maps of their maximum shear stress predicted by StressUnet (bottom)

### C. Comparisons

As can be seen in Fig. 4, the blocks used to compress the specimen were visible through the disc and ring, appearing as dark rectangles at the top and bottom of the fields. The unwrapping algorithm interpreted these dark areas as phase jumps and produced the noisy discontinuous zones seen at the top and bottom of the samples. StressUnet interpreted these areas as patches of low stress. Using smaller samples, a larger sensor or smaller blocks could reduce this effect, but how stress is distributed around the load points is generally not of much interest, so in many cases, it could be sufficient to simply remove these areas from the mask.

The magnitudes of the maximum shear stress were approximately a factor of three lower in the stress maps produced by the phase-shifting technique than those produced by StressUnet. The value for  $F_\sigma$  obtained from the disc was lower than the literature value of  $130 \text{ kNm}^{-1} \text{ Fringe}^{-1}$  by approximately a factor of 3.5 [29]. It is possible that our material was not prepared out of PMMA, but out of a different photoelastically sensitive material. In that case, the magnitudes of the stress maps produced by StressUnet for the experimental images are incorrect, as StressUnet assumes PMMA specimens. This issue could be resolved by ensuring the specimen is prepared from PMMA in future experiments.

The process of producing maximum shear stress maps with StressUnet was much less complicated and time-consuming than with the phase shifting technique. In the case of the disc under diametric compression, the PST produced a much more accurate map of maximum shear stress. Whilst it failed to do so successfully for the ring, it seems that, once improvements are made to the unwrapping process, the PST has the potential to produce more accurate stress maps than StressUnet when evaluated on experimental data. Should such unwrapping improvements be made, this would confirm that StressUnet is better suited to quick, relatively rough measurements, whereas the ten-step PST is better suited to situations where stress maps are required to be highly accurate and precise.

### VIII. CONCLUSION

In this work, two methods for stress analysis with digital photoelasticity, the ten-step phase-shifting technique with a phase unwrapping algorithm and StressUnet, a convolutional neural network based on U-Net, were compared and contrasted. We demonstrated that both methods performed inconsistently when evaluated on experimentally obtained data for the cases of a circular disc and ring under diametric compression and that StressUnet performed robustly when evaluated on the large, diverse validation set of computer-generated isochromatic images, achieving high structural similarity with the reference stress maps. We highlighted the advantages and limitations of each method, noting that producing stress maps with StressUnet was much faster and less complex than with the phase-shifting technique, requiring just one image to be captured compared to the PST's ten, but that the phase-shifting technique had the potential to produce more accurate results and did so in the case of the disc. We proposed implementing AQGPU to improve the unwrapping algorithm, increasing the number of training epochs as an improvement to StressUnet, and adjustments to the experimental setup that could improve the accuracy of both methods. To further investigate and compare these methods, it would be desirable to evaluate them on a more diverse set of experimental cases, varying the shape and light source.

### REFERENCES

- [1] William Moews, Samuel J. Ling, Jeff Sanny, William Moews, Samuel J. Ling, and Jeff Sanny. 12.3 Stress, Strain, and Elastic Modulus - University Physics Volume 1 | OpenStax, September 2016. URL <https://openstax.org/books/university-physics-volume-1/pages/12-3-stress-strain-and-elastic-modulus>. Book Title: University Physics Volume 1 Publisher: OpenStax.
- [2] Dominic J. Bello and Frederick A. Leckie. Strength and Stiffness of Engineering Systems. Mechanical Engineering Series. Springer US, Boston, MA, 2009. ISBN 978-0-387-49473-9 978-0-387-49474-6. doi:10.1007/978-0-387-

- 49474-6. URL <https://link.springer.com/10.1007/978-0-387-49474-6>.
- [3] H. T. Jessop and C. Snell. Photoelasticity and Aircraft Design. *Aeronautical Quarterly*, 3(3):161–172, November 1951. ISSN 0001-9259. doi:10.1017/S0001925900000603. URL <https://www.cambridge.org/core/journals/aeronautical-quarterly/article/abs/photoelasticity-and-aircraft-design/D0D82AF93E9B5CC671176932CA4090EB>. Publisher: Cambridge University Press.
- [4] Jonathan Barés, Serge Mora, Jean-Yves Delenne, and Thierry Fourcaud. Experimental observations of root growth in a controlled photoelastic granular material. *EPJ Web of Conferences*, 140:14008, 2017. ISSN 2100-014X. doi:10.1051/epjconf/201714014008. URL <http://www.epj-conferences.org/10.1051/epjconf/201714014008>.
- [5] William Prager. Numerical Methods of Stress Analysis. In Franz L. Alt and Morris Rubinoff, editors, *Advances in Computers*, volume 10, pages 253–273. Elsevier, January 1970. doi:10.1016/S0065-2458(08)60438-6. URL <https://www.sciencedirect.com/science/article/pii/S0065245808604386>.
- [6] David Brewster. III. Experiments on the depolarisation of light as exhibited by various mineral, animal, and vegetable bodies, with a reference of the phenomena to the general principles of polarisation. By David Brewster, LL. D. F. R. S. Edin and F. S. A. Edin. In a letter addressed to the Right Hon. Sir Joseph Banks, Bart. K. B. P. R. S. *Philosophical Transactions of the Royal Society of London*, 105:29–53, January 1997. doi:10.1098/rstl.1815.0004. URL <https://royalsocietypublishing.org/doi/10.1098/rstl.1815.0004>. Publisher: Royal Society.
- [7] Max Mark Frocht. *Photoelasticity*. Wiley, New York, 1941.
- [8] Max Mark Frocht. *Photoelasticity*. Wiley, New York, 1948.
- [9] K. Ramesh. *Developments in Photoelasticity: A renaissance*. IOP Publishing, October 2021. ISBN 978-0-7503-2472-4. doi:10.1088/978-0-7503-2472-4. URL <https://iopscience.iop.org/book/mono/978-0-7503-2472-4.pdf>.
- [10] M. Ramji and K. Ramesh. Stress Separation in Digital Photoelasticity Part A - Photoelastic Data Unwrapping and Smoothing. *Journal of Aerospace Sciences and Technologies*, pages 5–15, 2008. ISSN 2584-1351. doi:10.61653/joast.v60i1.2008.811. URL <http://www.joast.org/index.php/joast/article/view/811>.
- [11] G. M. Brown and J. L. Sullivan. The computer-aided holophotoelastic method. *Experimental Mechanics*, 30(2):135–144, June 1990. ISSN 1741-2765. doi:10.1007/BF02410239. URL <https://doi.org/10.1007/BF02410239>.
- [12] Yann LeCun, Yoshua Bengio, and Geoffrey Hinton. Deep learning. *Nature*, 521(7553):436–444, May 2015. ISSN 1476-4687. doi:10.1038/nature14539. URL <https://www.nature.com/articles/nature14539>. Number: 7553 Publisher: Nature Publishing Group.
- [13] Juan Carlos Briñez-de León, Mateo Rico-García, Alejandro Restrepo-Martínez, and John W. Branch. Isochromatic-art: a computational dataset for evaluating the stress distribution of loaded bodies by digital photoelasticity. 4, June 2020. doi:10.17632/z8yhd3sj23.4. URL <https://data.mendeley.com/datasets/z8yhd3sj23/4>. Publisher: Mendeley Data.
- [14] Olaf Ronneberger, Philipp Fischer, and Thomas Brox. U-Net: Convolutional Networks for Biomedical Image Segmentation. In Nassir Navab, Joachim Hornegger, William M. Wells, and Alejandro F. Frangi, editors, *Medical Image Computing and Computer-Assisted Intervention – MICCAI 2015*, Lecture Notes in Computer Science, pages 234–241, Cham, 2015. Springer International Publishing. ISBN 978-3-319-24574-4. doi:10.1007/978-3-319-24574-4\_28.
- [15] Weiliang Zhao, Guanglei Zhang, and Jiebo Li. Accuracy improvement of demodulating the stress field with StressUnet in photoelasticity. *Applied Optics*, 61(29):8678–8687, October 2022. ISSN 2155-3165. doi:10.1364/AO.464466. URL <https://opg.optica.org/ao/abstract.cfm?uri=ao-61-29-8678>. Publisher: Optica Publishing Group.
- [16] Eugene Hecht. *Optics*, Global Edition. Pearson Education, Limited, Harlow, UNITED KINGDOM, 2016. ISBN 978-1-292-09696-4. URL <http://ebookcentral.proquest.com/lib/durham/detail.action?docID=5174663>.
- [17] E.J. Hearn. Experimental Stress Analysis. In *Mechanics of Materials 2*, pages 166–192. Elsevier, 1997. ISBN 978-0-7506-3266-9. doi:10.1016/B978-075063266-9/50007-X. URL <https://linkinghub.elsevier.com/retrieve/pii/B978075063266950007X>.
- [18] O. Mohr. Über die Darstellung des Spannungszustandes und des Deformationszustandes eines Körperelementes und über die Anwendung derselben in der Festigkeitslehre. *Der Civilingenieur*, 28(2):113–156, 1882.
- [19] Polymer Retarder Film | Edmund Optics, . URL <https://www.edmundoptics.co.uk/f/polymer-retarder-film/14827/>.
- [20] Spectral Response, . URL <https://maxmax.com/spectral-response.htm>.
- [21] Calculating the Emission Spectra from Common Light Sources, . URL <https://www.comsol.com/blogs/calculating-the-emission-spectra-from-common-light-sources/>.
- [22] Mounted Colour Filter Set - Pack of 6, . URL <https://www.philipharris.co.uk/product/physics/waves/light-waves/mounted-colour-filter-set-pack-of-6-/b8a46127>.
- [23] William W. Macy. Two-dimensional fringe-pattern analysis. *Applied Optics*, 22(23):3898, December 1983. ISSN 0003-6935, 1539-4522. doi:10.1364/AO.22.003898. URL <https://opg.optica.org/abstract.cfm?URI=ao-22-23-3898>.
- [24] Kaiming He, Xiangyu Zhang, Shaoqing Ren, and Jian Sun. Deep Residual Learning for Image Recognition. In *2016 IEEE Conference on Computer Vision and Pattern Recognition (CVPR)*, pages 770–778, June 2016. doi:10.1109/CVPR.2016.90. URL <https://ieeexplore.ieee.org/document/7780459>. ISSN: 1063-6919.
- [25] Zhou Wang, A.C. Bovik, H.R. Sheikh, and E.P. Simoncelli. Image quality assessment: from error visibility to structural similarity. *IEEE Transactions on Image Processing*, 13(4):600–612, April 2004. ISSN 1941-0042. doi:10.1109/TIP.2003.819861. URL <https://ieeexplore.ieee.org/abstract/document/1284395>?casa\_token=OXXmIbR90ggAAAAA:Oeg1-5ocu06Wb7-qTSKWR9i7j1Cr8fxax0zoMJ\_09u80ZkZBBQhDRiIVoEiPNiKLXMRvLBAYMqQ. Conference Name: IEEE Transactions on Image Processing.
- [26] Diederik P. Kingma and Jimmy Ba. Adam: A Method for Stochastic Optimization, January 2017. URL <http://arxiv.org/abs/1412.6980> [cs].
- [27] Zhangyu Ren, Qi Zhang, Yang Ju, and Huimin Xie. Determination of the full-field stress and displacement using photoelasticity and sampling moiré method in a 3D-printed model. *Theoretical and Applied Mechanics Letters*, 12(6):100380, November 2022. ISSN 2095-0349. doi:10.1016/j.taml.2022.100380. URL <https://www.sciencedirect.com/science/article/pii/S2095034922000605>.
- [28] M. Ramji and K. Ramesh. Adaptive Quality Guided Phase Unwrapping Algorithm for Whole-Field Digital Photoelastic Parameter Estimation of Complex Models. *Strain*, 46(2):184–194, 2010. ISSN 1475-1305. doi:10.1111/j.1475-1305.2008.00431.x. URL <https://onlinelibrary.wiley.com/doi/abs/10.1111/j.1475-1305.2008.00431.x>. eprint: <https://onlinelibrary.wiley.com/doi/pdf/10.1111/j.1475-1305.2008.00431.x>.
- [29] Wei-Chih Wang. Photoelasticity. *Department of Mechanical Engineering, University of Washington*.

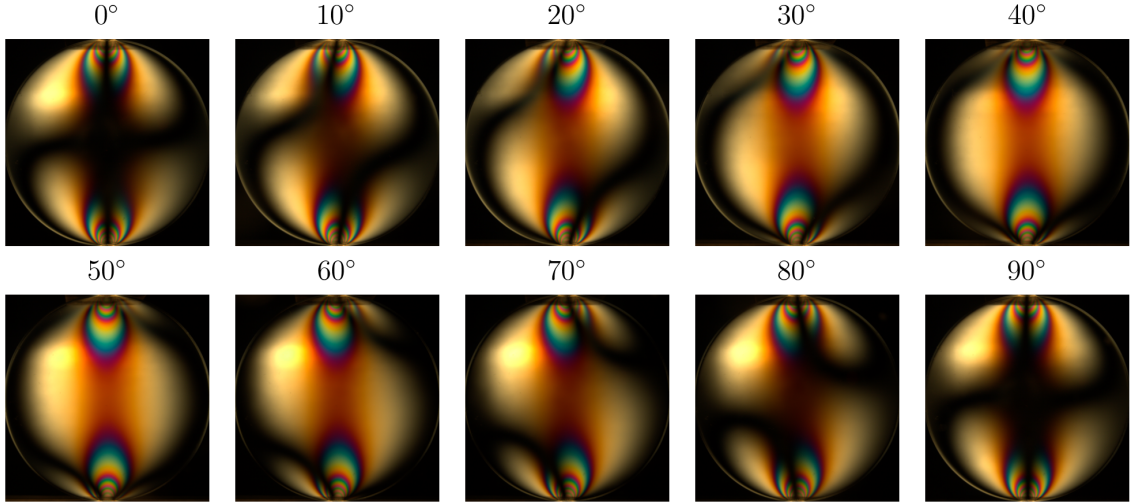


**FIG. 11:** Experimentally obtained images of a ring under diametric compression in a dark-field plane polariscope. The angle of the polariser is indicated, and the polariser-analyser system is kept crossed.

#### Appendix A: Errors

The light used for the ten-step PST was approximately monochromatic. Its relative spectral content illustrated in Fig. 3 is approximated by a normal distribution with mean  $\lambda_{\text{peak}}$  given by the peak wavelength and standard deviation  $\sigma_\lambda$  calculated from the full width at half maximum FWHM as

$$\sigma = \frac{1}{2\sqrt{2\ln 2}} \text{FWHM}. \quad (\text{A1})$$

FWHM is defined as the difference between the two wavelength values at which the spectral content is 0.5.

$\alpha_N$ , the error in central fringe-order  $N_c$ , was calculated as the standard deviation of the 100-pixel square kernel centred on the centre of the disc,

$$\alpha_N = \sqrt{\frac{1}{100} \sum_{i=1}^{100} (N_i - N_c)^2}, \quad (\text{A2})$$

where  $N_i$  denotes the fringe-order at pixel  $i$ , and  $N_c$  the mean fringe-order over the kernel.

The error  $\alpha_F$  associated with the material stress-fringe value  $F_\sigma$  was determined as

$$\alpha_F = F_\sigma \sqrt{\left(\frac{\alpha_P}{P}\right)^2 + \left(\frac{\alpha_D}{D}\right)^2 + \left(\frac{\alpha_N}{N_c}\right)^2} \quad (\text{A3})$$

where  $\alpha_D$  and  $\alpha_P$  give the experimentally obtained errors in diameter  $D$  and compressive force  $P$ , respectively.

#### Appendix B: Isotropic Point Determination Data

The data collected to identify the isotropic points in the disc and ring are presented in Fig. 11 and Fig. 12, respectively.

#### Appendix C: PST Data

The data collected for the disc and ring ten-step PST are presented in Fig. 13 and Fig. 14, respectively.

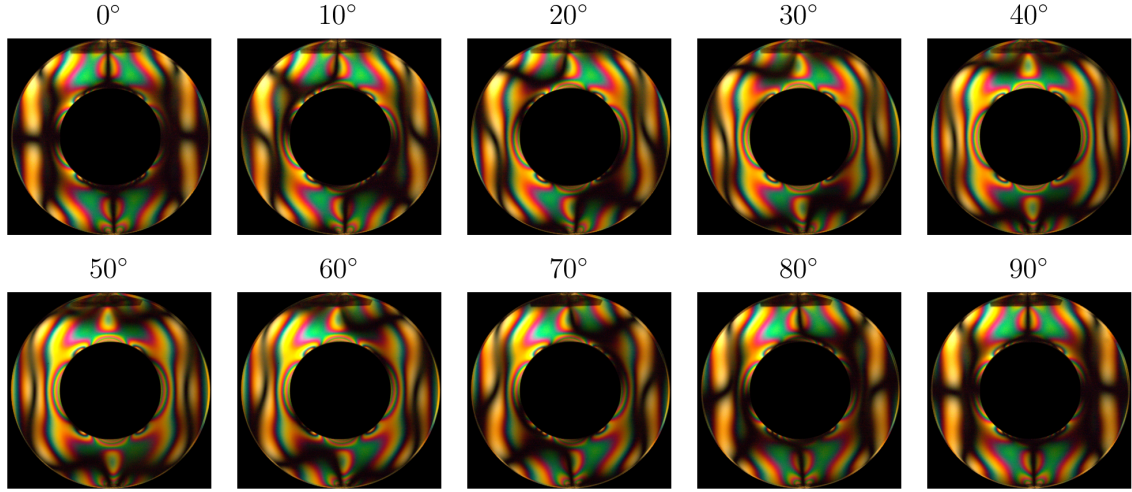


**FIG. 12:** Experimentally obtained images of a disc under diametric compression in a dark-field plane polariscope. The angle of the polariser is indicated, and the polariser-analyser system is kept crossed.

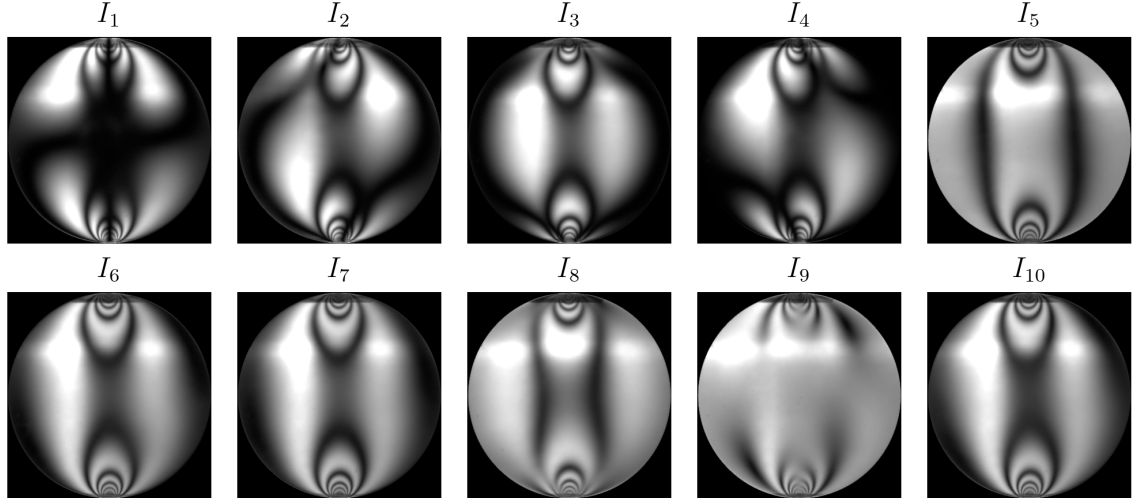


**FIG. 13:** Experimentally obtained images of the disc under diametric compression used in the ten-step PST.

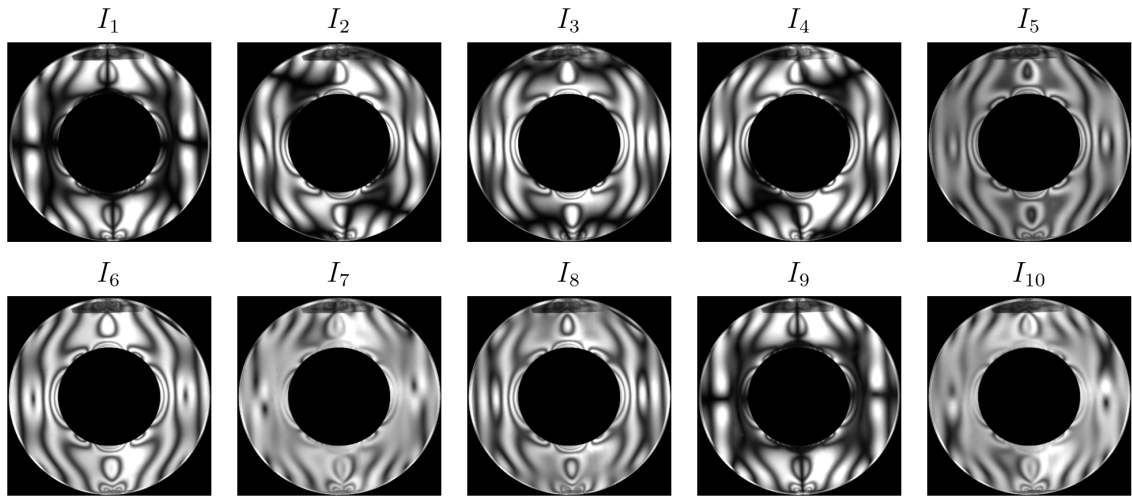
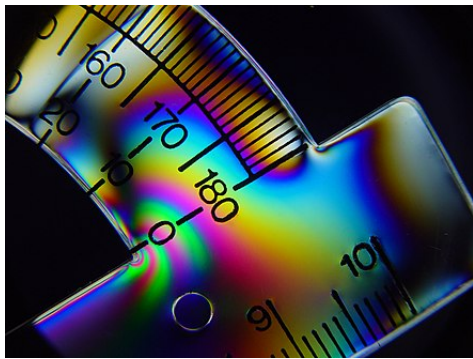


**FIG. 14:** Experimentally obtained images of the ring under diametric compression used in the ten-step PST.

**SCIENTIFIC SUMMARY FOR A GENERAL AUDIENCE**

Understanding how shapes behave when compressed or stretched is of vital importance in many areas. Consider, for example, Tower Bridge supporting the weight of thousands of people and cars each day, or the wings of a Boeing 737 balancing the weight of the aircraft with the forces from the air around it. Were either of these to break or lose shape whilst in use, the results could be catastrophic. To avoid such disasters, engineers have several techniques at their disposal. One approach is to use supercomputers to simulate the shapes. Unfortunately, whilst effective, supercomputers are expensive to run and complicated to use.



A simpler, cheaper approach takes advantage of photoelasticity, the same phenomenon responsible for the rainbow pattern you may have observed when using a plastic protractor, as above, or eating lunch with plastic cutlery. With the help of just a basic camera, a lamp and some standard optical equipment, engineers can understand how complex shapes behave under force, enabling them to build reliable wings, bridges and much more. In this work, we attempt to further speed up and simplify the process by implementing a machine-learning technique borrowed from the medical field, and compare it to a more traditional approach.

**200 words**

"Plastic Protractor Polarized" by Nevit Dilmen is licensed under CC BY-SA 2.0